Cell geometry dependent changes in plasma membrane order direct stem cell signalling and fate

Thomas C. von Erlach[1,2,3], Sergio Bertazzo[1,2,3], Michele A. Wozniak[4], Christine-Maria Horejs[1,2,3], Stephanie A. Maynard[1,2,3], Simon Attwood[1,2], Benjamin K. Robinson[1,2], Hélène Autefage[1,2,3], Charalambos Kallepitis[1,2,3], Armando Del Rio Hernandez[1,2], Christopher S. Chen[4,5], Silvia Goldoni[1,2,3*], Molly M. Stevens[1,2,3*]

[1]Department of Bioengineering Imperial College London, London SW7 2AZ, UK

[2]Institute of Biomedical Engineering, Imperial College London, London SW7 2AZ, UK

[3]Department of Materials, Imperial College London, London SW7 2AZ, UK

[4]Department of Bioengineering, University of Pennsylvania, Philadelphia, PA 19103, USA; [5]Biomedical Engineering, Boston University, Boston 02215; The Wyss Institute for Biologically Inspired Engineering, Harvard University, Boston 02115.

[*]Correspondence should be addressed to S.G. (e-mail: s.goldoni22@gmail.com) and M.M.S. (e-mail: m.stevens@imperial.ac.uk)

Cell size and shape affect cellular processes such as cell survival, growth and differentiation[1-4], thus establishing cell geometry as a fundamental regulator of cell physiology. The contributions of the cytoskeleton, specifically actomyosin tension, to these effects have been described, but the exact biophysical mechanisms that translate changes in cell geometry to changes in cell behaviour remain mostly unresolved. Using a variety of innovative materials techniques, we demonstrate that the nano-structure and lipid assembly within the cell plasma membrane are regulated by cell geometry in a ligand-independent manner. These biophysical changes trigger signalling events involving the serine/threonine kinase Akt/PKB that direct cell geometry dependent mesenchymal stem cell differentiation. Our study defines a central regulatory role by plasma membrane ordered lipid raft microdomains in modulating stem cell differentiation with potential translational applications.

Studies based on proteomics and FRET imaging suggest that cytoskeletal proteins interact and associate with plasma membrane ordered lipid raft microdomains[5], which are important regulators of cell signalling[6]. Using model membranes, it was proposed that the formation of the actin cytoskeleton network induces membrane phase separation and heterogeneity, both indicators of lipid raft formation[7]. In line with this observation, events resulting in enhanced formation of cytoskeletal networks, such as integrin engagement with the extracellular matrix and focal adhesion formation were found to increase membrane order[8], a biophysical hallmark of lipid rafts[10] as previously demonstrated[9]. We hypothesized that changes in cytoskeletal networks resulting from changes in cell architecture modulate lipid rafts independently of soluble extracellular cues. As a result, the biophysical state of the cytoskeleton directly regulates the activity of cell signalling proteins associated with plasma membrane micro-domains. Although this has been shown in differentiated cell types, the relationship between rafts and the cytoskeleton in mesenchymal stem cell function and fate is

largely unknown. In order to investigate this, we cultured human mesenchymal stem cells (hMSCs) on surfaces micropatterned with fibronectin islands of triangular, square and circular geometries with identical surface area (1350 μm^2). Cells adhered specifically to fibronectin and displayed distinct morphologies and cytoskeletal arrangement dictated by the geometric feature of the island (Fig. 1a and b). Fluorescence intensity heatmaps of F-actin and myosin IIa highlighted differences in cell contractility amongst the three geometries (Fig. 1c). Analysis of the compliance of living cells by atomic force microscopy (AFM) revealed significant differences in cell shape dependent cell stiffness between triangular and circular as well as square and circular cells with higher stiffness measured in triangular and square cells correlating with cell contractility in these geometries (Fig. 1d). The AFM data shows for the first time a link between cell shape and cell elasticity which is independent of cell adhesion area. To observe the 3D structural arrangement of the cell plasma membrane we developed a new method to obtain serial sections of cells *in situ* using focused-ion-beam coupled to imaging (Fig.2a). 3D reconstructions of plasma membranes brought to light remarkably different topographies across cell geometries down to the nano-scale (Fig. 2b). This observation correlated with a significantly increased number of membrane invaginations in the size range of 50-100 nm, resembling caveolae, a subset of lipid rafts, in triangular compared to circular cells (Fig. 2c and d, non-treated). These data suggest a connection between changes in cell contractility and caveolae formation. Interestingly, it was previously reported, that white blood cells and neurons lack caveolae but still have planar shaped lipid rafts[11]. This suggests that caveolae are a product of surface area demand and supports the notion that cells in a state of lower cytoskeletal contractility assemble less caveolae on the plasma membrane. By micropatterning cells in different shapes but with the same adhesion area we can decouple area and cytoskeletal contractility. To investigate the connection between cell contractility and caveolae formation further we analysed the number of caveolae in triangular, square and

circular hMSC in the presence of Cytochalasin D, a mycotoxin that interferes with actin polymerisation. Disrupting the actin cytoskeleton abolished cell shape dependent differences in caveolae abundance (Fig. 2d, CytoD). Furthermore, treating hMSC with Y27632, a ROCK (Rho-associated kinase) inhibitor that blocks myosin IIa light chain phosphorylation and consequently actomyosin contraction, led to a similar effect (Fig. 2d). As caveolae are cholesterol-rich structures, we used methyl-β-cyclodextrin (MβCD), a cholesterol sequestering agent, which disrupts the integrity of these membrane microdomains without affecting the cell shape and spreading[12](Fig. S1). Treating hMSC with MβCD significantly lowered the number of caveolae across cell shapes compared to non-treated cells and erased geometry dependent differences as the actin cytoskeleton modulators Cytochalasin D and Y27632 (Fig. 2d; representative images as in c of treatment groups are in Fig. S2). Interestingly however, treatment with MβCD does not change cell shape and spreading on fibronectin islands and F-actin staining reveals less actin bundling and focal organization in square and triangular cells (Fig. S1) supporting the interdependence between the actin cytoskeleton and caveolae. This interdependence has been shown in neurons where disruption of lipid rafts by cholesterol depletion results in aberrant axonal growth and guidance[13].

We further investigated the relationship between geometrical cues and lipid rafts with total internal reflection fluorescence (TIRF) microscopy. For this purpose, we used FITC-conjugated cholera toxin B subunit (CTB), which binds to GM1 gangliosides and serves as a lipid raft marker and fluorescent filipin III. CTB was shown to bind specifically to lipid rafts[14], and filipin III binds cholesterol[15], a characteristic and preferential component of lipid rafts. We detected significantly higher FITC-CTB signal on the plasma membrane of triangular and square hMSCs compared to round cells (2 and 1.5 fold, respectively) and the intensity of fluorescent filipin III was around 20% and 10% higher in triangular and square cells, respectively, compared to round cells (Fig. 3a and b). The chemical heterogeneity of the plasma

membrane across cell geometries correlates with the structural heterogeneity observed by *in situ* FIB microscopy where the underlying biophysical mechanism and structure-function relationship are yet to be understood. Plasma membrane invaginations detected by FIB are likely caveolae based on their size and their sensitivity to MβCD treatment. Because caveolae, a subtype of lipid rafts[16], are caveolin-1 positive structures, we measured caveolin-1 expression on the plasma membrane of patterned hMSC. Quantification of TIRF images revealed around 20% more caveolin-1 expressed on the plasma membrane of triangular and square cells compared to round cells (Fig. 3a and b) in line with the quantification of caveolae-like invaginations by *in situ* FIB microscopy shown in Figure 2a-d. By using three distinct markers, we showed that cell geometry regulates CTB and Filipin III positive cholesterol rich microdomains concomitant with increases in caveolin-1 expression. This indicates that cell geometry regulates the amount of plasma membrane lipid rafts. In line with this hypothesis, CD71 (transferrin receptor), which is associated to non-raft membrane domains, was equally expressed on the plasma membrane of triangular and round cells (Fig. 3c and d). To link the state of cytoskeletal contractility to caveolar lipid rafts abundance, we imaged CTB and caveolin-1 in the presence or absence of Y27637. Disrupting the RhoA pathway abolished cell shape dependent differences in both caveolae and lipid rafts abundance (Fig. 3e and f) indicating that cytoskeletal contractility can regulate plasma membrane biophysics in an extracellular signalling independent fashion. As expected, sequestering cholesterol with MβCD also erased cell shape dependent modulation of lipid rafts (Fig. 3e and f). It appears that MβCD treatment causes redistribution of Cav-1 from the periphery to internal regions within the substrate facing plasma membrane of circular hMSCs suggesting potential cytoskeletal rearrangement and internalization of Cav-1 positive lipid rafts (Fig. S4). Furthermore, the effect of hMSCs cell shape on plasma membrane order was investigated by analysing giant plasma membrane vesicles (GPMVs) isolated from triangular,

square and circular micropatterns using C-laurdan, a polarity sensitive membrane dye, and multiphoton microscopy[17]. GPMVs from triangular cells displayed the highest membrane order (Fig. 3g and h) confirming our observation that lipid raft markers are more abundant in these cells. As a control experiment for this technique we analysed GPMVs from hMSC grown in a tissue culture flask in the presence or absence of MβCD (Fig. S5).

Considering the cell signalling and endocytosis function of lipid rafts and caveolae[16], we investigated whether the observed cell geometry dependent changes could trigger downstream signalling driving cell behaviour. It was recently reported that the activity of the serine/threonine kinase Akt, also known as protein kinase B (PKB), a central node in cell signalling, is regulated by its association with lipid rafts[18]. Studies revealed that lipid rafts facilitate recruitment to the inner leaflet of the plasma membrane and subsequent activation of Akt and its activator PDK1 (pyruvate dehydrogenase lipoamide kinase isozyme 1) [19,20] and that MβCD mediated cholesterol depletion abolishes Akt signalling in keratinocytes[21]. Activated by growth factors, cytokines and ligand-independent stimuli, Akt and PDK-1 are recruited to the plasma membrane resulting in the phosphorylation of Akt at T308 and subsequent signal transduction[22]. We measured the phosphorylation level of Akt at its regulatory site T308 in differently shaped micropatterned hMSC (950 cells/shape) via In-Cell Western (ICW) (Fig. 4a). In line with the differential lipid raft assembly in cells displaying high cytoskeletal contractility, we found significantly higher Akt T308 phosphorylation in triangular and square cells compared to circular cells (Fig. 4f, control). To corroborate these data and to validate the signalling from ICW was specific, we ran a western blot for pan Akt and phospho-Akt T308 using the same antibodies used in ICW (Fig. 4e). Western blot also showed a decrease in Akt T308 phosphorylation in round cells compared to triangular cells (full blot images in Fig. S5). Because Akt recruitment to the plasma membrane is important for its activation, we quantified Akt abundance on the cell surface by TIRF microscopy (Fig. 4b). Significantly more Akt

protein was found on the surface of triangular and square cells compared to round cells (Fig. 4c). This result supports the data on Akt phosphorylation and highlights the existence of a connection between cell geometry and Akt signalling activation. To investigate cell shape dependent Akt association to lipid rafts, we analysed the correlation of Akt expression to CTB signal by TIRF microscopy. Due to the resolution limit of TIRF microscopy, the colocalization is limited to plasma membrane micro-domains and not to nano-domains. We found increased co-localisation of CTB and Akt as well as Akt and PDK1 as compared to CAV-1-Akt, cSRC-Akt, CD71-CAV-1 and CD71-CTB, quantified by Pearson's coefficient, supporting the existence of an interaction between Akt and PDK1 in lipid rafts (Fig. 4d).

Confident in the quantitative nature of ICW using the chosen antibodies, we further analysed the connection between cytoskeletal contractility, lipid rafts and Akt T308 phosphorylation using chemical inhibitors. Disrupting lipid rafts by cholesterol depletion using MβCD or the cholesterol binding agent ~~and lipid raft inhibitor~~ filipin III[21,23] reduced Akt T308 phosphorylation in high contractility geometries leading to abolishment of shape dependent differences (Fig. 4f). A similar effect on Akt T308 phosphorylation was observed when cell contractility was inhibited with Y27632 and Cytochalasin D (Fig. 4f). Furthermore, the Akt allosteric inhibitor MK2206[24] also erased cell shape driven Akt T308 phosphorylation (Fig. S7). Importantly, MK2206 blocks the PH domain of Akt which is required for lipid raft association. Taken together, these data demonstrate the existence of a previously unexplored mechanism of cell geometry dependent Akt activation mediated by cell contractility and lipid raft formation.

In order to gain some understanding of the molecular mechanism behind Akt activation by changes in cell shape, we investigated the role of the Akt upstream activator phosphatidylinositol-3 kinase (PI3K). PI3K mediates conversion of membrane phosphatidylinositol 4,5-bisphosphate (PI(4,5)P2) to phosphatidylinositol 3,4,5-trisphosphate

(PI(3,4,5)P3), which recruits both Akt and its activator PDK-1 to the plasma membrane by direct interaction[25]. We overexpressed a plasma membrane-targeted, constitutively active PI3K in hMSC. As expected, engineered cells display higher level of Akt phosphorylation compared to control cells (Fig. S8). Interestingly, hMSC with increased PI3K activity did not display any significant difference in cell shape dependent Akt phosphorylation compared to control cells indicating that the observed mechanism is independent of the amount of PIP3 on the plasma membrane (Fig. 4g). On the contrary, inhibition of PI3K activity by LY294002, an inhibitor of the P110 catalytic subunit, abolished shape dependent Akt T308 phosphorylation, indicating that the presence of PIP3 is required (Fig. 4f, LY). Additional protein kinases can be involved in this mechanism as LY294002 retains non-selective activity. The non-normalized results of Akt T308 phosphorylation are shown in Fig. S8.

Lastly, we investigated whether this newly identified lipid raft and cell contractility dependent mechanism had a functional effect in regulating stem cell differentiation. Micropatterned hMSC cultured in mixed adipogenic and osteogenic differentiation medium confined to have low and high cytoskeletal contractility, differentiated preferentially into adipocytes and osteoblasts, respectively, (Fig. 5a-c) as previously published[2,3,26]. Differentiation was assessed by staining with OilRedO and for alkaline phosphatase activity following 7 days in culture. Data were obtained by generating binary images with colour deconvolution (Fig. S10). Inhibition of cell contractility by Y27632 and Cytochalasin D led to the abolishment of cell shape differences since adipogenic differentiation increased by several fold in cell geometries with higher contractility (Fig. 5d). Remarkably, inhibiting lipid rafts with MβCD erased differences in lineage commitment dictated by cell shape and treating with filipin III resulted in a significant increase in adipogenesis in triangular and square cells (Fig. 5d). These data bring to light the existence of a previously unknown mechanism that links lipid rafts formation to hMSC differentiation. Importantly, treatment with the selective Akt

allosteric inhibitor MK2206 shifted overall hMSC differentiation towards adipogenesis resulting in no significant cell geometry dependent differences (Fig. 5d). These data define Akt as a major player in cell geometry dependent osteogenesis. We propose that a high cell contractility state favours lipid rafts formation and/or stability, and this in turn triggers Akt recruitment to the plasma membrane, pathway activation and osteogenic differentiation. In line with data presented in Figure 4g, increased PI3K activity did not change cell geometry dependent differentiation (Fig. 5e). Interestingly, when we performed *in situ* FIB microscopy of whole hMSC cell cross-sections, we observed the presence of characteristic lipid vacuoles (Fig. 5f). Round hMSC carried a higher number of these structures further supporting their preferential adipogenic phenotype (Fig. 5g). This phenotype is somewhat dependent on cytoskeletal contractility and presence of lipid rafts as the treatment with CytoD and MβCD reduced the differences across shapes (Fig. 5g).

To conclude, by using innovative materials and imaging techniques, we were able to investigate the cell-substrate interface and study plasma membrane morphology in 3D at the nano-scale level. We discovered a mechanism by which cell geometry regulates cell signalling via modulation of plasma membrane order. Changes in the plasma membrane due to geometric cues affect stem cell fate through a newly identified signalling mechanism involving Akt. Our data suggest a central role for lipid rafts in regulating cell behaviour and we propose that this mechanism allows cells to rapidly respond to changes in tissue mechanics and prepare for the integration of complex signals. Our findings expand the knowledge around tissue homeostasis mechanisms and also have broad implications for regenerative medicine and tissue engineering applications[27,28].

Acknowledgements

We would like to thank Hans Markus Textor and Fabian Anderegg (ETH Zurich) for providing silicon masters for micro-contact printing as well as Stephen Rothery for training and guidance

regarding TIRF microscopy (FILM facility at Imperial College London). T.v.E. was supported by an EPSRC DTA Ph.D. award. S.B. was supported by the Rosetrees Trust and the Stoneygate Trust and the Junior Research Fellowship scheme at Imperial College London. M.M.S. would like to thank ERC starting grant "Naturale" for funding under grant agreement no. 206807 and a Wellcome Trust Senior Investigator Award (098411/Z/12/Z).

Author Contributions

T.E. designed experiments, developed the substrates and conducted experiments, analysed and interpreted the data and wrote the manuscript. S.B. designed and carried out ion and electron microscopy experiments and analysed the data. M.W. conducted viral transfection experiments and revised the manuscript. C.K. performed 3D plasma membrane reconstruction and analysis. B.R and S.A. conducted AFM measurements. C.H. carried out western blots. C.C. revised the manuscript and consulted in experimental design. A.D.R.H. revised the manuscript and supervised S.A. H.A. helped with hMSC cultivation and differentiation experiments and revised the manuscript. S.M. helped with cell micropattern preparations, revised the manuscript. S.G. supervised the project, helped in experimental design, data analysis and interpretation and co-wrote the manuscript. M.M.S. supervised the project, co-wrote the manuscript and helped in experimental design and data interpretation.

Competing Financial Interest

The authors declare no competing financial interests.

Methods

Generation of micropatterned substrates. Stamps were made by replica casting polydimethylsiloxane (PDMS, Sylgard 184; Dow Corning, Midland, MI, USA) against a silicon master made by photolithography (gift from Markus Textor). PDMS pre-polymer was poured over the silicon master and cured at 60 °C overnight. The elastomeric stamp bearing the negative pattern of the master was peeled off and stored dry in a closed well plate at room temperature. Stamps were sonicated for 30 minutes in ethanol, rinsed three times with distilled water, blown dry under nitrogen, oxidized in air plasma for 1 minutes (200 mtorr) (Plasma Prep 5, Gala Instruments) and used for contact printing immediately. To allow adsorption of proteins, plasma-activated stamps were immersed for 1 hour in 50 µg/mL bovine fibronectin (sigma) in phosphate-buffered saline (PBS). Stamps were blown dry by compressed air and placed in conformal contact with the substrate (non-treated polystyrene multi-dish, Nunclon Surface) for 60 seconds before being peeled off. Subsequently, substrates were immersed in 0.4 % (w/v) Pluronic F127 (Sigma) in PBS for 2 hours, and carefully rinsed with water without allowing the surface to dry. Micropatterns for TIRF were generated by using silanized glass as a substrate for cell micropattern preparation according to a protocol published previously[29].

Culture of human mesenchymal stem cells and differentiation protocol. Human mesenchymal stem cells (hMSCs) (PromoCell) were cultured in mesenchymal stem cell growth medium (PromoCell) under standard cell culture conditions (37°C, 5 % CO_2). For experiments, cells were detached by using 0.25 % (v/v) Trypsin-EDTA solution (Invitrogen) and seeded in serum free growth medium at a density of 13000 cells/ cm^2 on the micropatterned substrate. After allowing cells to adhere for 2 hours, substrate was washed with PBS and media were replaced with serum containing media.

Antibodies and reagents. Mouse monoclonal anti-phospho-Akt (T308) (1:200), anti-phospho-Akt (Ser 473), polyclonal rabbit anti Akt (1:300), polyclonal rabbit anti myosin IIa light chain (1:400), monoclonal rabbit anti CD71, monoclonal rabbit anti Src, monoclonal rabbit anti PDK-1 as well as monoclonal mouse anti phospho myosin IIa light chain (1:100) were all purchased from Cell Signaling Technology. GAPDH was bought from Ambion. FITC conjugated Cholera Toxin B subunit (1:50) as well as filipin III from Streptomyces Filipinensis (1:10) were purchased from Sigma. Alexa Fluor®488 and Alexa Fluor®568 phalloidin (1:300) and DAPI (4',6-diamidino-2-phenylindole) were all obtained from Molecular Probes (Invitrogen). Polyclonal rabbit anti caveolin-1 (1:400) was purchased from Abcam. Secondary antibodies anti-mouse Alexa Fluor®568 (1:400) and anti-rabbit Fluor®488 (1:400) were bought from Molecular Probes. Infrared secondary antibodies, IRdye 680RD goat anti-mouse IgG and IRdye 800CW anti-rabbit (both 1:1000) were purchased from LiCor. For inhibitor studies, the following concentrations were used: 2.5 µM Y27632, 40 nM Cytochalasin D (both from Sigma), 3 µM MK-2206 (Active Biochemicals), 0.5 mM methyl-β-cyclodextrin (Santa Cruz Biotechnology), 0.5 µM filipin III and 20 µM LY294002 (both from Cayman Chemicals). Concentrations were determined based on cell morphology analysis. Y27632 and methyl-β-cyclodextrin were both solubilised in PBS, all other inhibitors were solubilised in DMSO according to manufacturer instructions. To exclude any effects of DMSO, control cell micropatterns were treated with DMSO (data not shown).

AdPI3K transfection. hMSCs were maintained in growth media (10 % (v/v) FBS in low-glucose DMEM). hMSCs were plated at a confluency of 13000 cells/ cm^2 overnight, and the next day infected with either GFP or PI3K-p110CAAX ("AdPI3K") virus for 5 hours. The following day, cells were trypsinized and 13000 cells/cm^2 were plated on Pluronic-blocked micropatterned substrates in the presence of growth media or differentiation media for Akt

activity assays or differentiation assays, respectively. Differentiation medium consisted of 1:1 adipogenenic:osteogenic media and was changed every 3 days. Adipogenic media contained 3 % (v/v) FBS, 1 % (v/v) penicillin-streptomycin, 500 µM IBMX, 2 µM rosiglitazone, 1 µM dexamethasone, 17 µM pantothenate, 33 µM biotin and 1 µM insulin in DMEM/F12. Osteogenic media contained 10 % (v/v) FBS, 1 % (v/v) penicillin-streptomycin, 100 nM dexamethasone, 250 µM ascorbic acid-2-phosphate and 10 mM β-glycerophosphate.

Giant plasma membrane vesicle (GPMV) isolation and analysis. GPMVs were isolated and analysed according to a previously published protocol[17]. Briefly, hMSCs were cultured on triangular, square and circular micropatterns for 24 hours, washed with GPMV buffer (10 mM HEPES, 150 mM NaCl, 2 mM $CaCl_2$, pH 7.4) and then incubated in GPMV isolation solution (25 mM Paraformaldehyde/2 mM Dithiothreitol in GPMV buffer) for 2 hours. Afterwards, solution was collected and transferred into bovine serum albumin coated vials. After 30 minutes, 50 µL from the bottom of the vial was transferred into a fresh bovine serum albumin coated vial and labelled with 1 µl of 0.2 mM solution of 6-Dodecanoyl-2-Dimethylaminonaphthalene (C-laurdan) (Molecular Probes) for 30 minutes.

Microscopy data analysis. For fluorescence analysis, cells grown on micropatterns were immunostained using standard procedures. Briefly, cells were fixed with 4 % (v/v) formalin in dH_2O (Sigma) for 15 minutes at room temperature, washed with PBS, permeabilised with 0.25 % (v/v) Triton-X-100/PBS for 2 minutes, washed with PBS and then blocked with 4 % (w/v) bovine serum albumin in PBS. Primary and secondary antibodies were incubated in blocking buffer for 1 hour at room temperature. For TIRF microscopy analysis using plasma membrane lipid markers CTB and Filipin III, samples were not permeabilised with Triton-X-100 to preserve the plasma membrane. Only single cells that were confined into the desired shape were selected by using the microscope in brightfield mode. An Olympus BX51 upright and an

Olympus inverted microscope were used to image fluorescence and phase contrast samples. For the histological analysis, cells were inspected by phase contrast to determine whether they expressed lineage specific markers based on what has been described previously[2]. Briefly, for patterned MSCs only single cells that adhered to the pattern were used for statistical analysis. Cells that contained lipid vacuoles stained red by OilRedO were counted as adipocyte specification. Cells that stained blue for alkaline phosphatase were counted as osteoblast committed cells. For additional quantitation we performed a colour deconvolution of all cells across a surface stained with both markers based on what was published earlier[2]. Briefly, raw RGB images acquired by phase contrast with a 20x objective were imported in ImageJ, background-subtracted and afterwards colour deconvoluted by a publicly available colour deconvolution plugin for ImageJ commonly used for separating similar histology stains (http://www.dentistry.bham.ac.uk/landinig/software/cdeconv/cdeconv.html) with colour-specific vectors adapted to the particular images. The resulting separated red and blue channels were binarised with a set threshold based on visual examination and subsequently quantified. For generating immunofluorescence heatmaps, MSCs cultured on the three different shapes were imaged on the same day using the same microscope and camera settings. Raw fluorescent images were background-subtracted in ImageJ, incorporated into a Z Hyperstack and the summarised intensity was calculated for heatmap generation. For Total Internal Reflection Fluorescence (TIRF) Microscopy, samples on glass substrate (glass bottom dish, MatTek Prod. Nb P35G-0-10-C) in PBS were imaged using a Zeiss Axiovert 200 manual inverted microscope with a 488 laser diode, an 100X/1.45W Alpha Plan Fluar objective and back illuminated EM-CCD camera (Hamamatsu C9100-13). Resulting 16 bit raw images were background-subtracted and binarised for quantification purposes using ImageJ software. For high resolution co-localisation analysis, background-subtracted TIRF microscopy images of 2 different channels were merged in one image. Then the Pearson Coefficient was analysed with ImageJ

using the JACoP Plugin (http://rsb.info.nih.gov/ij/plugins/track/jacop2.html). Multiphoton imaging of C-laurdan labelled giant plasma membrane vesicles (GPMVs) was performed with an inverted Olympus IX81 microscope with a 25X water immersion long working distance objective using a MaiTaiDeepSea Laser at 800 nm excitation and emission filtered at 410-440 nm as well as at 502-548 nm.

Western blot, In-Cell Western and immunofluorescence. For In-Cell Western, cellular proteins were quantitated *in situ* based on infrared intensity. Samples were immunolabelled with an infrared conjugated IgG secondary antibody using standard immunofluorescence protocol and imaged using an Odyssey Fc Infrared Imaging System (LiCor) in the highest resolution (21 µm). The resulting signal intensity was subsequently quantified by using the Odyssey CLx Image Studio Analysis Software. For western blots, Ad(GFP) and Ad(PI3K) cells were lysed in 25 mM HEPES, 75 mM NaCl, 1 % (v/v) NP-40, 1 mM EDTA, 1× Halt protease and phosphatase inhibitor cocktail (Thermo Scientific), and centrifuged at 14000RPM for 10 minutes at 4 °C. Lysates from cells on hydrogels were obtained with RIPA buffer (Sigma) containing protease inhibitors (Roche) and phosphatase inhibitors (Sigma). Protein concentration was determined by Precision Red Advanced Protein Assay (Cytoskeleton, Denver, CO). 10 µg of protein was separated by denaturing SDS–PAGE, transferred to PVDF membrane, blocked with 5 % (w/v) bovine serum albumin (BSA) in 0.3 % (v/v) Tween-20 in Tris-buffered saline, immunoblotted with primary antibodies (1:1000), and detected using horseradish peroxidase–conjugated secondary antibodies (1:5000; Jackson ImmunoResearch Laboratories) and SuperSignal West Dura (Pierce). Densitometric analysis was performed using a VersaDoc imaging system and QuantityOne software (Bio-Rad Laboratories), and statistically analysed using GraphPad Prism software. Western blot was performed using

infrared labelled secondary antibodies, scanned and analysed using the Odyssey imaging system and software (LiCor).

Atomic Force Microscopy (AFM) analysis. hMSCs were cultured on the three micropatterned shapes for 24 hours afterwards samples were analysed in the petri dish in PBS at room temperature by Atomic Force Spectroscopy. A Nanowizard I (JPK, Germany) Atomic Force Microscope (AFM) with an inverted microscope (IX-81, Olympus,Germany) was used for all measurements. We used MLCT-D levers (Bruker) with a nominal spring constant of 0.03N/m. For analysis cantilevers were calibrated immediately before use using the thermal noise method. Polystyrene Microspheres with a diameter of 15 µm (Life Technologies) were attached to AFM cantilever tips using a UV curable glue (Loctite 350, rs-online) as described elsewhere[30]. Force-displacement curves were analysed using a custom developed routine in Matlab (MathWorks). The contact point was identified by considering each point in the approach curve and fitting the Hertz model to the contact region and a constant value for the points thereafter. The point with the smallest error for the combined fits was identified as the contact point. The Young's modulus, E, was then determined for the contact region from this point onwards. Indentation was kept below 10% of the cell height to avoid substrate effects[24].

Focused Ion Bean (FIB) and Scanning Electron Microscopy (SEM) analyses. Micropatterned cells were fixed in a 4 % (v/v) formaldehyde (Sigma, BioReagent, ≥ 36.0 %) with 0.2 % (v/v) glutaraldehyde (EMS – Electron Microscopy Sciences) solution in PBS at room temperature for 15 minutes. Samples were washed three times with cacodilate buffer (EMS – Electron Microscopy Sciences) and osmicated with osmium tetroxide in 2 % (w/v) cacodilate buffer for 30 minutes. After that, samples were washed five times with deionized water and then dehydrated through a graded ethanol (Sigma, ACS reagent 99.5 %) series two

times for each concentration (20, 30, 40, 50 70, 80, 90, 100, 100, 100% (v/v)) for 2 minutes in each solution. After dehydration, samples were infiltrated with Epon Resin (EMS – Electron Microscopy Sciences) diluted in ethanol at 3:1, 2:1, and 1:1 for 1 hour each, and then overnight at 1:2. The solution was then replaced with pure resin, which was changed twice in the first 12 hours and then allowed to infiltrate again overnight. After that, the maximum amount of resin was removed and the bottom of the well plate (containing the cells) was detached and centrifuged at 5000rpm for 5 min. Samples were immediately placed in an oven at 60 °C and left to cure overnight. Samples were secured to a SEM aluminium sample holder with carbon tape and silver paint applied to the area immediately surrounding the sample (to maximise conductivity), and then coated with 5nm of chromium in a sputter coater (QuorumTechnologies model K575X). Following the coating procedure, samples were introduced into an SEM/Focused Ion Bean (Carl Zeiss - Auriga) with gallium ion bean operated at 30 kV. A region over the cells with approximately 15 x 5 x 2 µm (length x height x depth) was milled using 4 nA current. After that, the region exposed by the first milling was polished with 240 pA current and imaged by a backscattering detector with the electron bean operating at 1.5 V. To generate a 3D-surface model, individual high resolution *in situ* cross-section electron micrographs of micropattered cells were stacked using MATLAB®. From these volume datasets an iso-surface was extracted based on polygonal abstraction. The surface roughness parameters including Roughness Average, Root Mean Square (RMS), Maximum Valley Depth, Maximum Peak Height and Peak-Peak Height were then calculated according to the ISO (International Organization for Standardization) as described in the ISO 25178-2:2012. The area between the substrate surface and substrate facing cell plasma membrane was calculated by using the Image J software.

Statistical Analysis. All data were analysed by one-way ANOVA followed by a Tukey and Bonferroni post hoc analysis.

Data Availability. Raw data is available upon request from m.stevens@imperial.ac.uk.

References

1. Chen, C. S., Mrksich, M., Huang, S., Whitesides, G. M., & Ingber, D. E. Geometric Control of Cell Life and Death. *Science* **276**, 1425–1428 (1997).
2. Kilian, K. a, Bugarija, B., Lahn, B. T. & Mrksich, M. Geometric cues for directing the differentiation of mesenchymal stem cells. *Proceedings of the National Academy of Sciences of the United States of America* **107**, 4872–7 (2010).
3. McBeath, R., Pirone, D. M., Nelson, C. M., Bhadriraju, K. & Chen, C. S. Cell shape, cytoskeletal tension, and RhoA regulate stem cell lineage commitment. *Developmental Cell* **6**, 483–495 (2004).
4. Aragona, M., Panciera, T., Manfrin, A., Giulitti, S., Michielin, F., Elvassore, N., Dupont, S., et al. A mechanical checkpoint controls multicellular growth through YAP/TAZ regulation by actin-processing factors. *Cell* **154**, 1047–59 (2013).
5. Head, B. P., Patel, H. H., & Insel, P. A. Interaction of membrane/lipid rafts with the cytoskeleton: impact on signaling and function: membrane/lipid rafts, mediators of cytoskeletal arrangement and cell signaling. *Biochimica et Biophysica Acta*, **1838**(2), 532–45 (2014).
6. Simons, K. & Toomre, D. Lipid rafts and signal transduction. *Nature reviews. Molecular Cell Biology* **1**, 31–9 (2000).
7. Liu, A. P. & Fletcher, D. A. Actin polymerization serves as a membrane domain switch in model lipid bilayers. *Biophysical Journal* **91**, 4064–70 (2006).
8. Gaus, K., Le Lay, S., Balasubramanian, N. & Schwartz, M. Integrin-mediated adhesion regulates membrane order. *The Journal of Cell Biology* **174**, 725–34 (2006).
9. Head, B. P., Patel, H. H., Roth, D. M., Murray, F., Swaney, J. S., Niesman, I. R., Farquhar, M. G., Insel, P. A. Microtubules and Actin Microfilaments Regulate Lipid

Raft / Caveolae Localization of Adenylyl Cyclase Signaling Components. *Journal of Biological Chemistry*, **281**(36), 26391–26399 (2006).

10. Lingwood, D. & Simons, K. Lipid rafts as a membrane-organizing principle. *Science* **327**, 46–50 (2010).

11. Head, B. P., & Insel, P. A. Do caveolins regulate cells by actions outside of caveolae? *Trends in Cell Biology*, **17**(2), 51–57 (2007).

12. Palazzo, A. F., Eng, C. H., Schlaepfer, D. D., Marcantonio, E. E., & Gundersen, G. G. Localized stabilization of microtubules by integrin- and FAK-facilitated Rho signaling. *Science*, **303**(5659), 836–9 (2004).

13. Kamiguchi, H. The region-specific activities of lipid rafts during axon growth and guidance. *Journal of Neurochemistry*, **98**(2), 330–335 (2006).

14. Blank, N., Schiller, M., Krienke, S., Wabnitz, G., Ho, A. D., & Lorenz, H.M. Cholera toxin binds to lipid rafts but has a limited specificity for ganglioside GM1. *Immunology and Cell Biology* **85**, 378–82 (2007).

15. Wüstner, D. Fluorescent sterols as tools in membrane biophysics and cell biology. *Chemistry and Physics of Lipids* **146**, 1–25 (2007).

16. Parton, R. G., & Simons, K. The multiple faces of caveolae. *Nature reviews. Molecular cell biology* **8**, 185–94 (2007).

17. Sezgin, E., Kaiser, H.-J., Baumgart, T., Schwille, P., Simons, K., & Levental, I. Elucidating membrane structure and protein behavior using giant plasma membrane vesicles. *Nature Protocols*, ***7*(6)**, 1042–51 (2012).

18. Gao, X. & Zhang, J. Spatiotemporal Analysis of Differential Akt Regulation in Plasma Membrane Microdomains. *Molecular Biology of the Cell* **19**, 4366–4373 (2008).

19. Lasserre, R., Guo, X.-J., Conchonaud, F., Hamon, Y., Hawchar, O., Bernard, A.-M., Soudja, S. M., et al. Raft nanodomains contribute to Akt/PKB plasma membrane recruitment and activation. *Nature Chemical Biology* **4**, 538–47 (2008).

20. Gao, X., Lowry, P. R., Zhou, X., Depry, C., Wei, Z., Wong, G. W., & Zhang, J. PI3K/Akt signaling requires spatial compartmentalization in plasma membrane microdomains. *Proceedings of the National Academy of Sciences of the United States of America* ***108***(35), 14509–14 (2011).

21. Calay, D., Vind-Kezunovic, D., Frankart, A., Lambert, S., Poumay, Y., & Gniadecki, R. Inhibition of Akt signaling by exclusion from lipid rafts in normal and transformed epidermal keratinocytes. *The Journal of Investigative Dermatology*, **130**(4), 1136–45 (2010).

22. Manning, B. D. & Cantley, L. C. AKT/PKB signaling: navigating downstream. *Cell* **129**, 1261–74 (2007).

23. Schnitzer, J. E., Oh, P., Pinney, E., & Allard, J. (1994). Filipin-sensitive caveolae-mediated transport in endothelium: Reduced transcytosis, scavenger endocytosis, and capillary permeability of select macromolecules. *Journal of Cell Biology*, **127**(5), 1217–1232 (1994).

24. Hirai, H., Sootome, H., Nakatsuru, Y., Miyama, K., Taguchi, S., Tsujioka, K., et al. MK-2206, an allosteric Akt inhibitor, enhances antitumor efficacy by standard chemotherapeutic agents or molecular targeted drugs in vitro and in vivo. *Molecular Cancer Therapeutics*, **9**(7), 1956–67 (2010).

25. Vanhaesebroeck, B., Stephens, L., & Hawkins, P. PI3K signalling: the path to discovery and understanding. *Nature reviews. Molecular cell biology* **13**, 195–203 (2012).

26. Müller, P., Langenbach, A., Kaminski, A., & Rychly, J. Modulating the Actin Cytoskeleton Affects Mechanically Induced Signal Transduction and Differentiation in Mesenchymal Stem Cells. *PLoS ONE*, **8**(7), 1–8 (2013).

27. Stevens, M. M. & George, J. H. Exploring and engineering the cell surface interface. *Science* **310**, 1135–8 (2005).

28. Place, E. S., Evans, N. D. & Stevens, M. M. Complexity in biomaterials for tissue engineering. *Nature Materials* **8**, 457–70 (2009).

29. Tan, J. L., Liu, W., Nelson, C. M., Raghavan, S. & Chen, C. S. Simple approach to micropattern cells on common culture substrates by tuning substrate wettability. *Tissue Engineering* **10**, 865–72 (2004).

30. Harris A. R., Charras G. T. Experimental validation of atomic force microscopy-based cell elasticity measurements. *Nanotechnology* **22**, 1-10 (2011).

Figure Captions

Fig. 1 Cell geometry induces changes in cytoskeletal arrangement and cell contractility. (a) Representative SEM micrographs of micropatterned hMSC. (b) Representative immunofluorescence images of hMSC stained for F-actin (green) and Dapi (blue). (c) Immunofluorescence intensity heat maps of myosin IIa and F-actin. Higher intensity is represented by a yellow/white colour. n = number of cells used for heat map generation. (d) Live cell stiffness measurement of triangular, square and circular cells by atomic force microscopy (AFM). 30 cells per condition were analysed. * equals $p<0.05$; *** equals $p<0.001$. Error bars represent S.E.M.

Fig. 2 Cell geometry regulates plasma membrane morphology and topography. (a) High resolution electron micrographs of cells *in situ* generated by focused ion beam microscopy. (I) SEM micrographs of triangular, square and circular micropatterned cells; (II) micropatterned cells sectioned in the middle by focused ion beam; (III) cross-section analysed with high magnification reveals cell geometry dependent morphology of plasma membrane facing the substrate. (b) Cross-section and 3D reconstruction of plasma membrane surface illustrated as topographical heatmap based on 60 cross-sections of triangular (top) and circular (bottom) cells. (c) High magnification micrographs focusing on the plasma membrane-substrate interface reveal the presence of membrane invaginations in the range of 50-100 nm resembling caveolae (yellow arrows). (d) Number of caveolae-like structures quantified from images as in c of control hMSC and cells treated as indicated. Data are obtained from 19 to 35 cross-section images from 3 to 6 cells per shape. * equals $p<0.05$. Data are presented as box plots to show values distribution; bottom and top of box represent 25% and 75%, respectively.

Fig. 3 Signal intensity of lipid raft markers is dependent on cell geometry. (a) Representative TIRF microscopy images of the plasma membrane-substrate interface. Cholera Toxin Subunit B (CTB) is a marker for lipid rafts and Filipin III stains for accumulation of cholesterol, a hallmark of lipid rafts. Caveolin-1 positive plasma membrane domains are a subtype of lipid rafts. (b) Quantification of TIRF images per condition and stain (n = 75-93 for CAV-1, n = 33-37 for Filipin III, n = 38-53 for CTB, n = 20-32 CD71). Box plots show complete data range, bottom and top of box represent 25% and 75%,

respectively. *** equals $p<0.001$, * equals $p<0.05$ (3 independent experiments). (c) Representative TIRF microscopy images of triangular and circular hMSC stained for CD71, a non-raft marker. (d) Quantification of 50 TIRF images of CD71 stained hMSC as in c. (e-f) Quantification of TIRF images of triangular and circular hMSC as in a, treated with either the ROCK inhibitor Y27632 or methyl-β-cyclodextrin (MβCD) (n = 35-46 for CTB and n = 29-42 for CAV-1). (g) Representative multiphoton images of C-laurdan stained giant plasma membrane vesicles (GPMVs) isolated from triangular, square or circular hMSCs with emission light filtered to select wavelengths representative of ordered (green) and disordered (red) phase. (h) Quantification of the ratio of fluorescence intensity of the ordered (green) and disordered (red) phase emission of GPMVs isolated from triangular, square or circular hMSCs (n = 51-123). Box plots show complete data range, bottom and top of box represent 25% and 75%, respectively. *** equals $p<0.001$ (3 independent experiments).

Fig. 4 Akt recruitment to the plasma membrane and activation are dependent on cell geometry. (a) Representative In-Cell Western (ICW) images of arrays of micropatterned hMSC. Cells were stained with phospho-AKT T308 and pan AKT antibodies. Bar = 1 mm. (b) Representative TIRF images of AKT. Bar = 20 μm. (c) Quantification of TIRF images per shape as in b, from 3 independent experiments. Box plots show complete data range, bottom and top of box represent 25% and 75%, respectively (n = 34-46). *** equals $p<0.001$, ** equals $p<0.01$ (d) Co-localisation analysis from TIRF images of markers indicated and Akt in triangular hMSC quantified by the Pearson's coefficient (n = 8-11). *** equals $p<0.001$. (e) Representative Western blot of phospho-AKT T308 and pan AKT of triangular and circular hMSC. GAPDH was used as loading control. Note that antibodies used in Western blot are the same as in ICW. (f) Quantification of data from ICWs as in a, of cells treated as indicated (CytoD = Cytochalasin D; LY= LY294002). (g) Quantification of phospho-AKT T308 and pan AKT by ICW of hMSC stably transfected to carry enhanced PI3K activity compared to GFP transfected control cells. Values are means ± S.D. * equals $p<0.05$, ** equals $p<0.01$ (3 independent experiments in duplicate).

Fig. 5 Lipid rafts and Akt signalling mediate cell geometry dependent hMSC differentiation. (a) Representative images of hMSC differentiated into either fat (OilRedO) or bone cells (alkaline

phosphatase activity). (b) Quantification of differentiation of micropatterned hMSC into either adipocytes or osteoblasts, following 7 days in the presence of a 1:1 mix of adipogenic and osteogenic differentiation medium. Compiled from cells from 7 independent experiments performed in duplicate (n = 364-392). Values are means ± S.D. *** equals $p<0.001$. (c) Frequency histograms of OilRedO and alkaline phosphatase activity corresponding to data shown in b. (d) Quantification of adipogenic and osteogenic fate as in a, of micropatterned hMSC treated as indicated. (e) Quantification of adipogenic and osteogenic fate of hMSC transfected with constitutively active PI3K. Values are means ± S.D. ** equals $p<0.01$. 100 cells per condition (3 independent experiments in duplicate). (f) Representative images of whole cell cross-sections of triangular, square and circular hMSC reveal the presence of characteristic lipid vacuoles (white round structures). Note the high density of lipid vacuoles in round hMSC supporting evidence that low cell contractility geometries favour adipogenesis. Cells are cultured in basal medium. (g) Quantification of lipid vacuoles from whole cell cross-sections as in f of control hMSC and cells treated as indicated. Data are obtained from 5 to 10 cells per shape. Data are presented as box plots to show values distribution; bottom and top of box represent 25% and 75%, respectively. ** equals $p<0.01$.

Figures

Figure 1:

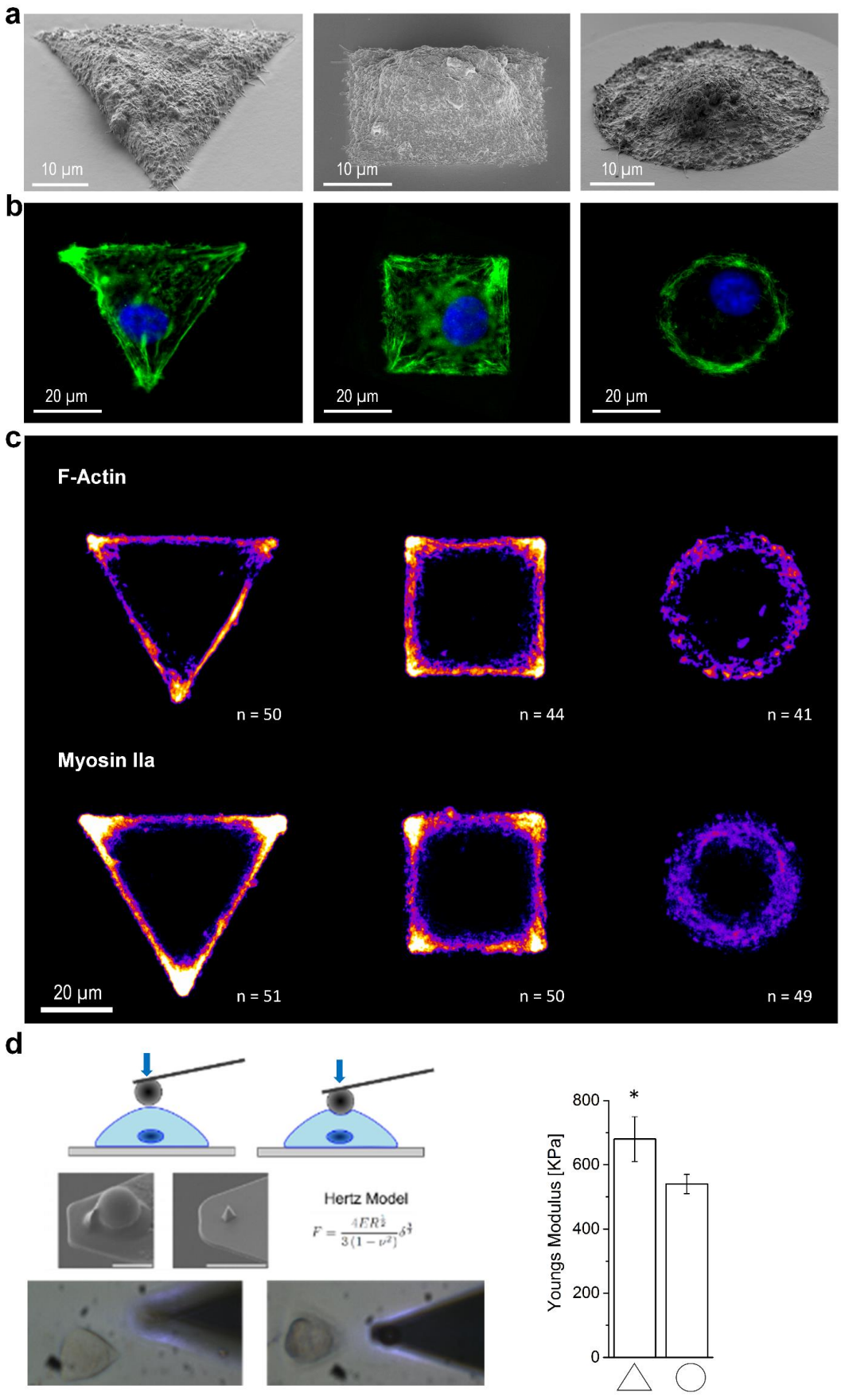
a
10 µm
10 µm
10 µm
b
20 µm
20 µm
20 µm
c
F-Actin
n = 50
n = 44
n = 41
Myosin IIa
20 µm
n = 51
n = 50
n = 49
d
Hertz Model
$F = \frac{4ER^{\frac{1}{2}}}{3(1-\nu^2)}\delta^{\frac{3}{2}}$
Youngs Modulus [KPa]
800
600
400
200
0
*

577

578

579 **Figure 2:**

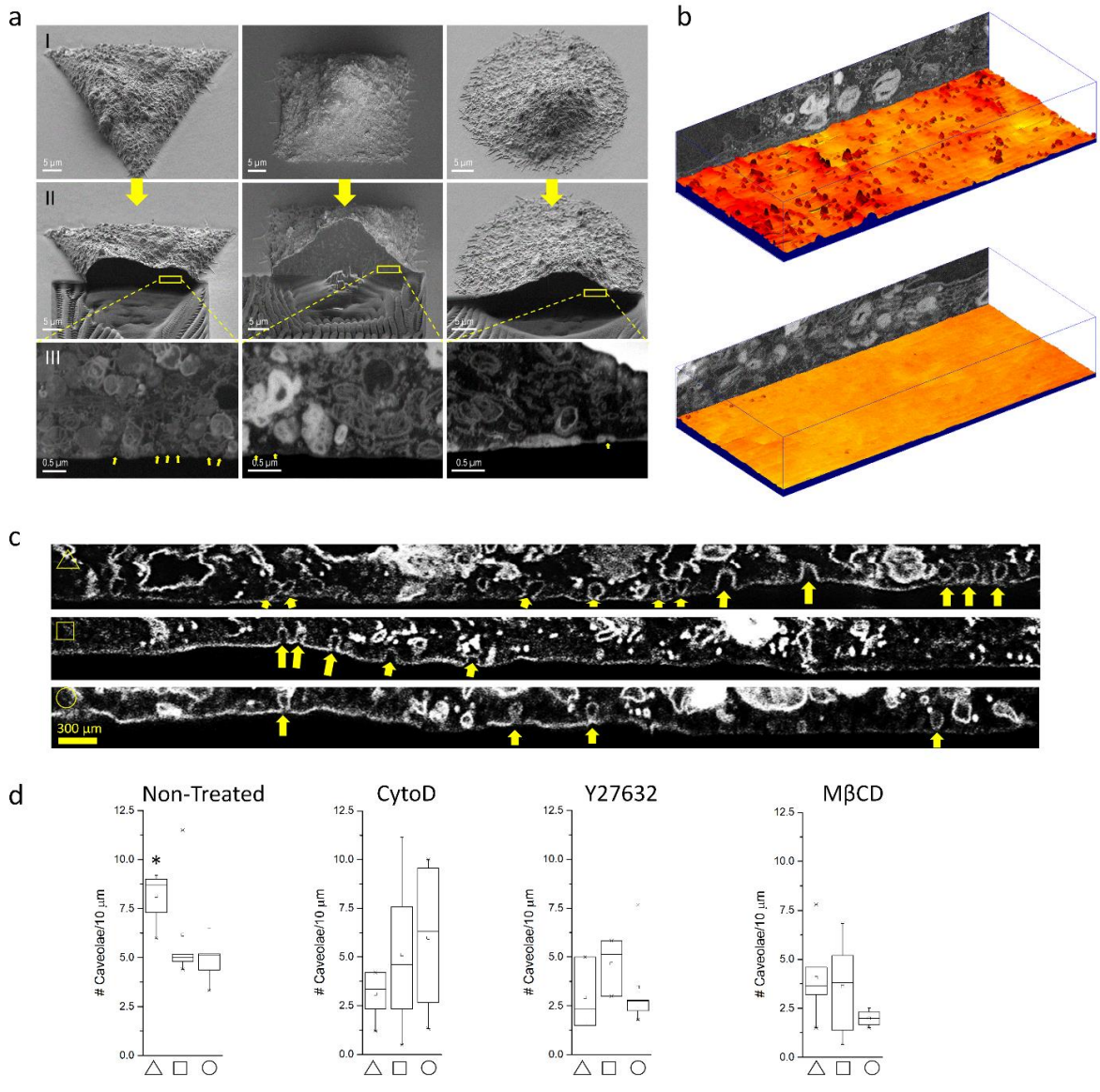

580

581

582 **Figure 3:**

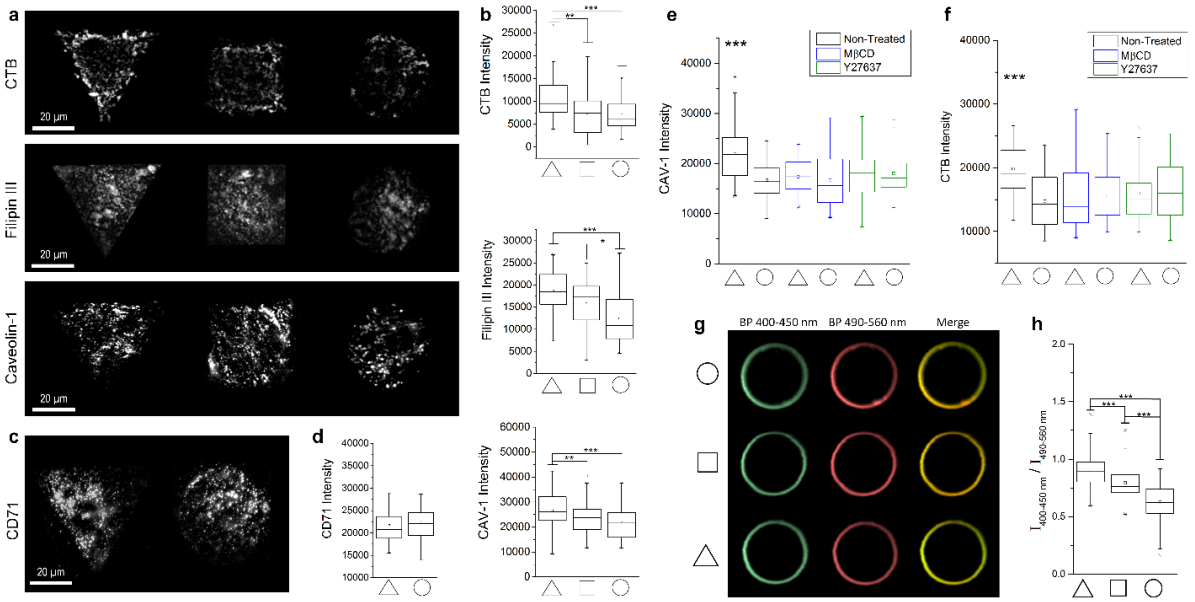

583

584

585 **Figure 4:**

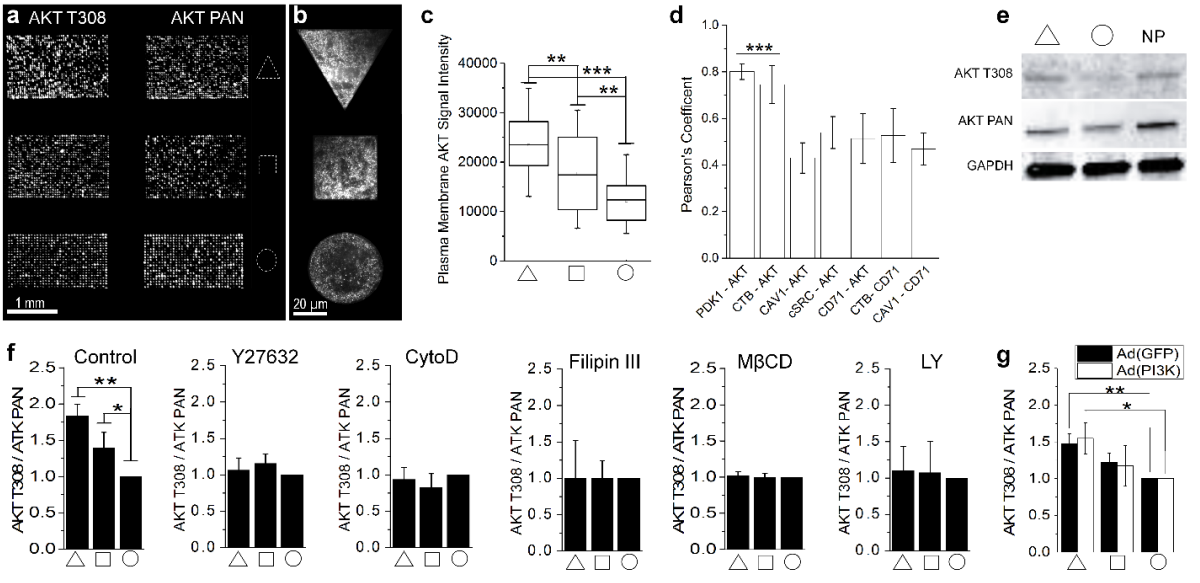

586

587

588 **Figure 5:**

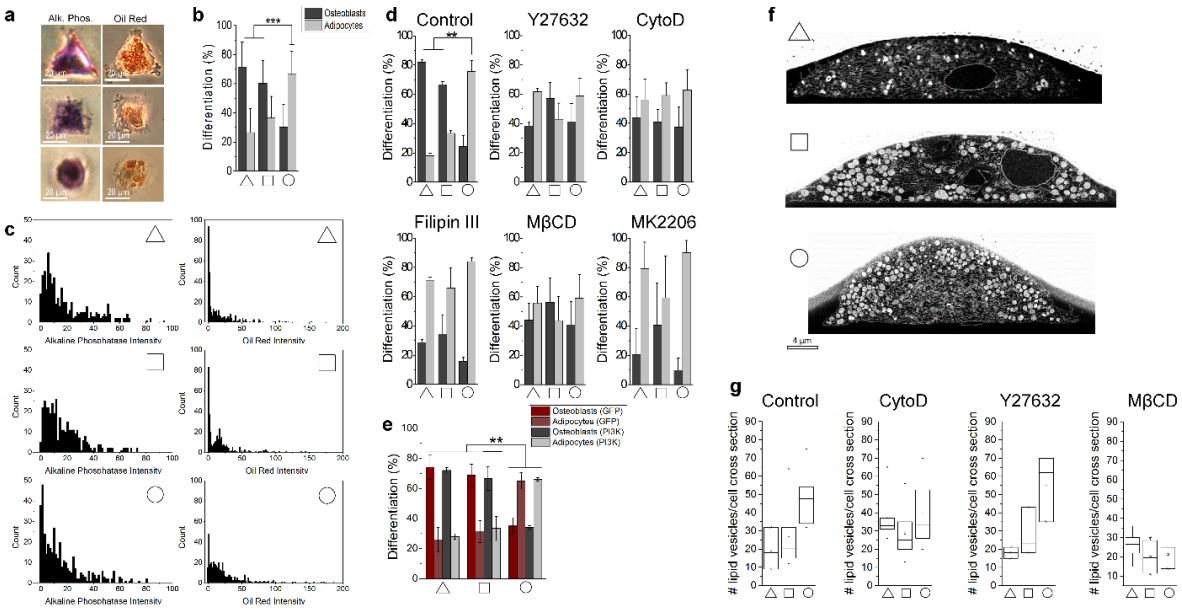
a
Alk. Phos.
Oil Red
b
Osteoblasts
Adipocytes
Differentiation (%)
c
Count
Alkaline Phosphatase Intensity
Oil Red Intensity
d
Control
Y27632
CytoD
Filipin III
MβCD
MK2206
e
Osteoblasts (GFP)
Adipocytes (GFP)
Osteoblasts (PI3K)
Adipocytes (PI3K)
f
4 μm
g
Control
CytoD
Y27632
MβCD
lipid vesicles/cell cross section

589

590